Accretion on to a binary from a polar circumbinary disc

Jeremy L. Smallwood [1,2]★ Stephen H. Lubow [3] and Rebecca G. Martin [2]

[1] *Center for Astrophysics, Space Physics, and Engineering Research, Baylor University, Waco, Texas 76798-7316, USA*
[2] *Department of Physics and Astronomy, University of Nevada, Las Vegas, 4505 South Maryland Parkway, Las Vegas, NV 89154, USA*
[3] *Space Telescope Science Institute, Baltimore, MD 21218, USA*

ABSTRACT

We present hydrodynamical simulations to model the accretion flow from a polar circumbinary disc on to a high eccentricity ($e = 0.78$) binary star system with near unity mass ratio ($q = 0.83$), as a model for binary HD 98800 BaBb. We compare the polar circumbinary disc accretion flow with the previously studied coplanar case. In the coplanar case, the circumbinary disc becomes eccentric and the accretion alternates from being dominant on to one binary member to the other. For the polar disc case involving a highly eccentric binary, we find that the circumbinary disc retains its initially low eccentricity and that the primary star accretion rate is always about the same as the secondary star accretion rate. Recent observations of the binary HD 98800 BaBb, which has a polar circumbinary disc, have been used to determine the value of the Hα flux from the brighter component. From this value, we infer that the accretion rate is much lower than for typical T Tauri stars. The eccentric orbit of the outer companion HD 98800 A increases the accretion rate on to HD 98800 B by $\sim$20 per cent after each periastron passage. Our hydrodynamical simulations are unable to explain such a low accretion rate unless the disc viscosity parameter is very small, $\alpha < 10^{-5}$. Additional observations of this system would be useful to check on this low accretion rate.

Key words: accretion, accretion discs – hydrodynamics – binaries: general – circumstellar matter.

1 INTRODUCTION

It is estimated that more than 40–50 per cent of stars in the Galaxy are in a binary pair (Duquennoy & Mayor 1991; Raghavan et al. 2010; Tokovinin 2014a, b). Circumbinary discs of gas and dust are common around young binary stars and are locations for planet formation. Misalignments between the circumbinary disc and the binary orbital plane are commonly observed (Czekala et al. 2019). The pre-main-sequence binary KH 15D has a circumbinary disc tilted by about 5°–16° (Chiang & Murray-Clay 2004; Smallwood et al. 2019; Poon, Zanazzi & Zhu 2021). The pre-main sequence circumtriple disc around the hierarchical triple star system, GW Ori, is misaligned by about 38° (Bi et al. 2020; Kraus et al. 2020; Smallwood et al. 2021a). The young binary IRS 43 has a circumbinary disc with an observed misalignment of about 60° (Brinch et al. 2016). The 6–10 Gyr old binary system, 99 Herculis, has a nearly polar (about 87°) debris ring (Kennedy et al. 2012; Smallwood et al. 2020).

A misaligned young system of particular interest is HD 98800. The system is at a distance of 47 pc (van Leeuwen 2007), and comprises two pairs of binaries, HD 98800 AaAb and HD 98800 BaBb (Zúñiga-Fernández et al. 2021). The two sets of binaries are orbiting each other with semimajor axis 54 au, eccentricity $e_{AB} = 0.52 \pm 0.01$ and orbital period of 246 ± 5 yr (Kennedy et al. 2019). The orbit of the BaBb binary is well constrained with a semimajor axis $a \simeq 1$ au and eccentricity $e = 0.785 \pm 0.005$. The masses of the two B-binary stars are $M_{Ba} = 0.699$ and $M_{Bb} = 0.582 \, M_{\odot}$ (Boden et al. 2005). The circumbinary disc was first thought to be coplanar to the binary

orbital plane (Andrews et al. 2010) but the later observations showed the disc to be misaligned. From their ALMA observations, Kennedy et al. (2019) modelled the dust and carbon monoxide measurements and inferred that the radial dust component extends from 2.5 ± 0.02 to 4.6 ± 0.01 au and the gas component extends from 1.6 ± 0.3 to 6.4 ± 0.5 au. Both the dust and gas components were found to be in a similar orientation. From these observations, the circumbinary disc has an inferred inclination to the binary orbital plane of either 48° or 90° (polar). The polar configuration is more likely since their disc modelling suggests that the alignment time of a 48° disc to reach polar is very short compared to the stars' age. Additional support of the polar configuration was provided by the small observed size of the inner cavity in the circumbinary disc that requires a nearly polar disc orientation (Franchini, Lubow & Martin 2019).

A misaligned circumbinary disc undergoes nodal precession. For a low initial inclination, the precession is around the binary angular momentum vector (e.g. Larwood et al. 1996) while for sufficiently high initial inclination, the precession is around the eccentricity vector. Dissipation causes the disc to evolve to either align coplanar to the binary orbital plane (Papaloizou & Lin 1995; Lubow & Ogilvie 2000; Nixon et al. 2011; Facchini, Lodato & Price 2013; Foucart & Lai 2014) or align perpendicular (i.e. polar) to the binary orbital plane (Aly et al. 2015; Martin & Lubow 2017; Lubow & Martin 2018; Martin & Lubow 2018; Zanazzi & Lai 2018).

The dynamics of a coplanar binary-circumbinary disc system has been the subject of many studies. The binary opens a central cavity in the circumbinary disc through the effects of its tidal torques (Artymowicz & Lubow 1994; Miranda & Lai 2015). Circumbinary gas flows into the cavity in the form of gas streams (e.g. Artymowicz & Lubow 1996; Günther & Kley 2002; Shi et al. 2012;

★ E-mail: drjeremysmallwood@gmail.com

D'Orazio, Haiman & MacFadyen 2013; Farris et al. 2014; Miranda, Muñoz & Lai 2017; Mösta, Taam & Duffell 2019; Muñoz, Miranda & Lai 2019). This flow is important in forming and/or replenishing circumstellar discs around each binary component. The properties of the circumbinary gas disc and flow in the central cavity vary with binary eccentricity and mass ratio. In this paper, we are concerned with the case of a high binary eccentricity and near unity mass ratio, as occurs for HD 98800 BaBb. For a high eccentricity binary with mass ratio close to unity in a coplanar system, previous simulations have shown that there are large modulations in the accretion rate towards an eccentric orbit binary occur on the time-scales of $1P_{orb}$ (where P_{orb} is the binary orbital period), due to time-varying gravitational forces from the eccentric orbit binary. In addition, the circumbinary disc acquires substantial eccentricity around such a binary (e.g. Lubow & Artymowicz 2000; Muñoz & Lai 2016; Muñoz et al. 2019). As a consequence of the apsidal precession of the eccentric disc around an eccentric orbit binary with mass ratio of unity, the binary member that accretes the most material alternates in time between the two stars (Muñoz & Lai 2016).

Less is known about the accretion process in the non-coplanar case. At a given radius, tidal torques are weaker in the non-coplanar case, giving rise to smaller central cavities (Lubow, Martin & Nixon 2015; Miranda & Lai 2015; Franchini et al. 2019). Tidal torques due to Lindblad resonances on a polar disc approach zero in the limit of unity binary eccentricity (Lubow & Martin 2018). Recently, Smallwood, Martin & Lubow (2021b) showed that non-coplanar gas streams develop in the central cavity of a moderately inclined (60°) circumbinary disc. In this paper, we explore the properties of a polar circumbinary disc and accretion on to the binary as a model for HD 98800 BaBb.

Recently, Zurlo et al. (2020) conducted a survey of 11 transitional discs with the SPHERE instrument (Beuzit et al. 2019) at the Very Large Telescope (VLT). Their purpose was to undertake the largest Hα survey dedicated to protoplanets in hopes of detecting circumplanetary discs. The observations were carried out using the Hα filter of the Zimpol rapid-switching imaging polarimeter (ZIMPOL; Schmid et al. 2018). The ZIMPOL is a subsystem in visible light which takes simultaneous images in the Hα narrow band filter and Hα continuum. One of the 11 systems that were observed was HD 98800 BaBb. No sub-stellar companions were detected around the binary; however, unexpectedly, an Hα flux was detected from the primary binary component Ba. No Hα flux was detected from the secondary. From the Hα flux, Zurlo et al. (2020) estimated a Hα luminosity and an accretion luminosity.

In Section 2, we discuss the setup of the hydrodynamical simulations. In Section 3, we compare the disc structure of the coplanar and polar discs, along with comparing the accretion rates on to the binary. In Section 4, we include the outer companion HD 98800 A companion in our hydrodynamical simulations. In Section 5, we calculate the mass accretion rate on to the primary component in HD 98800 BaBb from the polar circumbinary disc using the Hα emission observations from Zurlo et al. (2020). Finally, we present our concluding remarks in Section 6.

2 HYDRODYNAMICAL SIMULATION SETUP

This section describes the 3D hydrodynamical simulation setup of a circumbinary disc around the eccentric orbit binary, HD 98800 BaBb. To model the accretion rate on to each binary component, we use the smoothed particle hydrodynamical code PHANTOM (Lodato & Price 2010; Price & Federrath 2010; Price et al. 2018). We consider two different initial circumbinary disc orientations, coplanar, and polar.

PHANTOM has been successful in modeling misaligned circumbinary discs (e.g. Nixon 2012; Nixon, King & Price 2013; Doğan et al. 2015; Facchini, Juhász & Lodato 2018; Aly & Lodato 2020; Smallwood et al. 2020). The hydrodynamic discs that we model here are in the wave-like regime, meaning that the disc aspect ratio, H/R, is larger than the Shakura & Sunyaev (1973) α-viscosity coefficient. This is appropriate for protoplanetary discs. The consequence of this is that the warp induced in the disc by the binary torque propagates as a pressure wave with speed $c_s/2$ (Papaloizou & Pringle 1983; Papaloizou & Lin 1995), where c_s is the sound speed.

The binary is modelled with the mass and orbital parameters from Kennedy et al. (2019) that are given in Section 1. When a particle enters the accretion radius, it is considered accreted and the particle mass and angular momentum are added to the sink particle. For both the initially coplanar and the initially polar models, we consider accretion radii $R_{acc} = 0.25, 0.025, 0.01$ au. We examine various accretion radii of each binary component. The smallest accretion radius used is comparable to the size of the star. Table 1 gives a summary of all the hydrodynamical simulations.

The discs initially consist of 1×10^6 equal mass smoothed particle hydrodynamic (SPH) Lagrangian particles that are radially distributed from the inner disc radius R_{in} to the outer disc radius R_{out}. Observations show that the inner radius of the polar disc in HD 98800 BaBb is about 1.6 au (Kennedy et al. 2019), whereas a coplanar disc around the same binary would have a much larger inner truncation radius of about 3 au (Artymowicz & Lubow 1994). As discussed in Section 1, a misaligned circumbinary disc can radially extend closer to the binary due to the binary torque being weaker at a given radius. We initially set the inner radius to be $R_{in} = 4$ au in all of our simulations since this is larger than the tidal truncation radius in all cases. This allows the material to initially move inwards before the disc reaches a quasi-steady state. If the disc were to begin too close to the binary, there could be an initially artificially enhanced accretion rate on to the binary, resulting in lost disc mass.

The outer disc radius is set to $R_{out} = 6.4$ au, which is motivated by the observations (Kennedy et al. 2019). We simulate the observed gas disc mass of $M_d \sim 8 \times 10^{-7}$ M$_\odot$ for the system based on CO flux (e.g. Kennedy et al. 2019).[1] The mass of the disc must be small, since the disc is observed to be only a few degrees away from a 90° polar state, and a larger disc mass leads to a generalized polar state at lower levels of misalignment (Martin & Lubow 2019). This inferred disc mass limit for HD 98800 BaBb is not large enough for self-gravity to be important.

The disc viscosity is modelled by using the artificial viscosity α^{av}, which is implemented in PHANTOM (Lodato & Price 2010). The disc surface density profile is initially a power-law distribution $\Sigma \propto R^{-3/2}$. We adopt the locally isothermal equation of state of Farris et al. (2014) and set the sound speed c_s to be

$$c_s = c_{s0} \left(\frac{a_b}{M_1 + M_2} \right)^q \left(\frac{M_1}{R_1} + \frac{M_2}{R_2} \right)^q, \tag{1}$$

where R_1 and R_2 are the radial distances from the primary and secondary star, respectively, and c_{s0} is a constant determined by the disc aspect ratio scaling. This prescription for the sound speed distribution ensures that the primary and secondary star irradiation sets the

---

[1] The simulations are initially modelled with a mass of $M_d = 10^{-3}$ M$_\odot$, but we re-scale the masses in the simulations by a factor of 8×10^{-4}. We expect that this procedure is valid, since the disc mass should not play an essential role in the dynamics of the binary.

Table 1. Overview of the hydrodynamical simulations. The first column shows the simulation name. The second column denotes the initial disc orientation, either coplanar or polar and the third column represents the accretion radius for each binary component. The fourth and fifth columns show the time-averaged mass accretion rate over the last $400\,P_{\rm orb}$ on to the primary and secondary stars, respectively. The last column denotes whether the HD 98800 A companion is included.

| Simulation	Orientation	$R_{\rm acc}/{\rm au}$	$\dot{M}_{\rm acc}^{\rm avg}/({\rm M_\odot\,yr^{-1}})$ Primary	Secondary	Third Companion?
run1	Coplanar	0.25	1.15×10^{-10}	1.18×10^{-10}	No
run2	Coplanar	0.025	1.08×10^{-10}	9.44×10^{-11}	No
run3	Coplanar	0.01	1.06×10^{-10}	1.06×10^{-10}	No
run4	Polar	0.25	6.05×10^{-11}	4.90×10^{-11}	No
run5	Polar	0.025	4.58×10^{-11}	4.22×10^{-11}	No
run6	Polar	0.01	4.43×10^{-11}	4.35×10^{-11}	No
run7	polar	0.25	6.28×10^{-11}	5.31×10^{-11}	Yes

temperatures around the circumprimary and circumsecondary disc, respectively. For $R_1(R_2) \gg a$, the sound speed is set by the distance from the binary centre of mass. The disc aspect ratio H/R is set to be 0.1 at $R_{\rm in}$. With this prescription, the shell-averaged smoothing length per scale height $\langle h \rangle/H$ and the disc viscosity parameter α are constant over the radial extent of the disc (Lodato & Pringle 2007). We take the Shakura & Sunyaev (1973) $\alpha_{\rm SS}$ parameter to be 0.01. The circumbinary disc is initially resolved with average smoothing length $\langle h \rangle/H = 0.19$.

To model the circumstellar discs in PHANTOM that are fed by circumbinary gas, we would need to adopt the prescription detailed in Smallwood et al. (2021b) in which we artificially reduce the sound speed close to each binary component. This increases the viscous time-scale in the circumstellar discs and allows material to build up around the binary components. However, with this prescription we would not be able to simulate for the long time-scale required to model the quasi-steady state accretion rate from the circumbinary disc to the binary. Resolving bound material on short length-scales is quite computationally expensive. Therefore, we do not try to capture the formation of such discs in these hydrodynamical simulations, since the larger number of particles required to resolve the formation of circumstellar discs around each binary component would significantly increase the computational time. The circumstellar discs may buffer accretion on to the stars, but this effect is not included since we are not revolving the individual discs. There is no observational evidence of circumstellar discs around either of the binary components in HD 98800 BaBb (e.g. Kennedy et al. 2019), and therefore we focus on how much material is accreted on to the binary components.

3 COPLANAR AND POLAR DISC EVOLUTION

3.1 Circumbinary disc structure

We investigate the structure and evolution of both an initially coplanar and polar circumbinary discs around an eccentric binary. Fig. 1 shows the surface density profile at $t = 1000\,P_{\rm orb}$ for the coplanar and polar models (runs 1 and 4 from Table 1). The coplanar surface density profile is truncated at about 2–3 au, while the surface density profile for the polar disc extends inward to about 1 au. For a particular radius from the centre of mass of the binary, the tidal torque is stronger around a coplanar binary than a polar binary. As expected (see Section 1), the polar disc's inner edge extends closer to the binary than the coplanar disc. We also show the maximum orbital radius of the secondary component in the disc's plane for both coplanar and polar disc orientations. For the
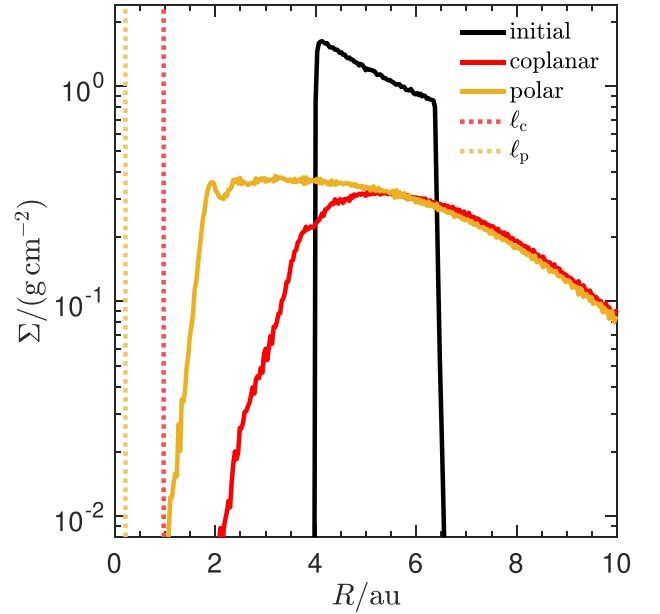
Figure 1. The disc surface density profile at time $t = 1000\,P_{\rm orb}$ for a coplanar disc (red, run1 from Table 1), and polar disc (yellow, run4). The black line gives the initial distribution. The vertical dotted lines show the closest approach of the secondary companion in the plane of the disc, measured from the initial center of mass of the binary. The red dotted line shows this distance for the coplanar binary, ℓ_c, and the yellow dotted line shows this distance for the polar binary, ℓ_p. The inner edge of the polar disc is closer in than the coplanar disc.

coplanar disc, this distance is $\ell_c = 0.97$ au. For the polar disc, this distance is measured from the initial center of mass of the binary when the binary components are in the plane of the disc, which is $\ell_p = 0.21$ au.

We further investigate the disc eccentricity and surface density for the two disc configurations. The top row in Fig. 2 shows the radial disc eccentricity evolution for the coplanar disc (run1 from Table 1) versus the polar disc (run4) and the bottom row shows the radial disc surface density as a function of time. There is heightened eccentricity growth around 2–3 au for the duration of the simulation for a coplanar disc. The patches of high eccentricity at < 2 au are in the central gap region (seen from the bottom-left panel) where the gas streams flow. The polar-orientated disc shows no heightened eccentricity growth except at the inner disc edge. From the surface density renderings, we see more material closer to the binary in the
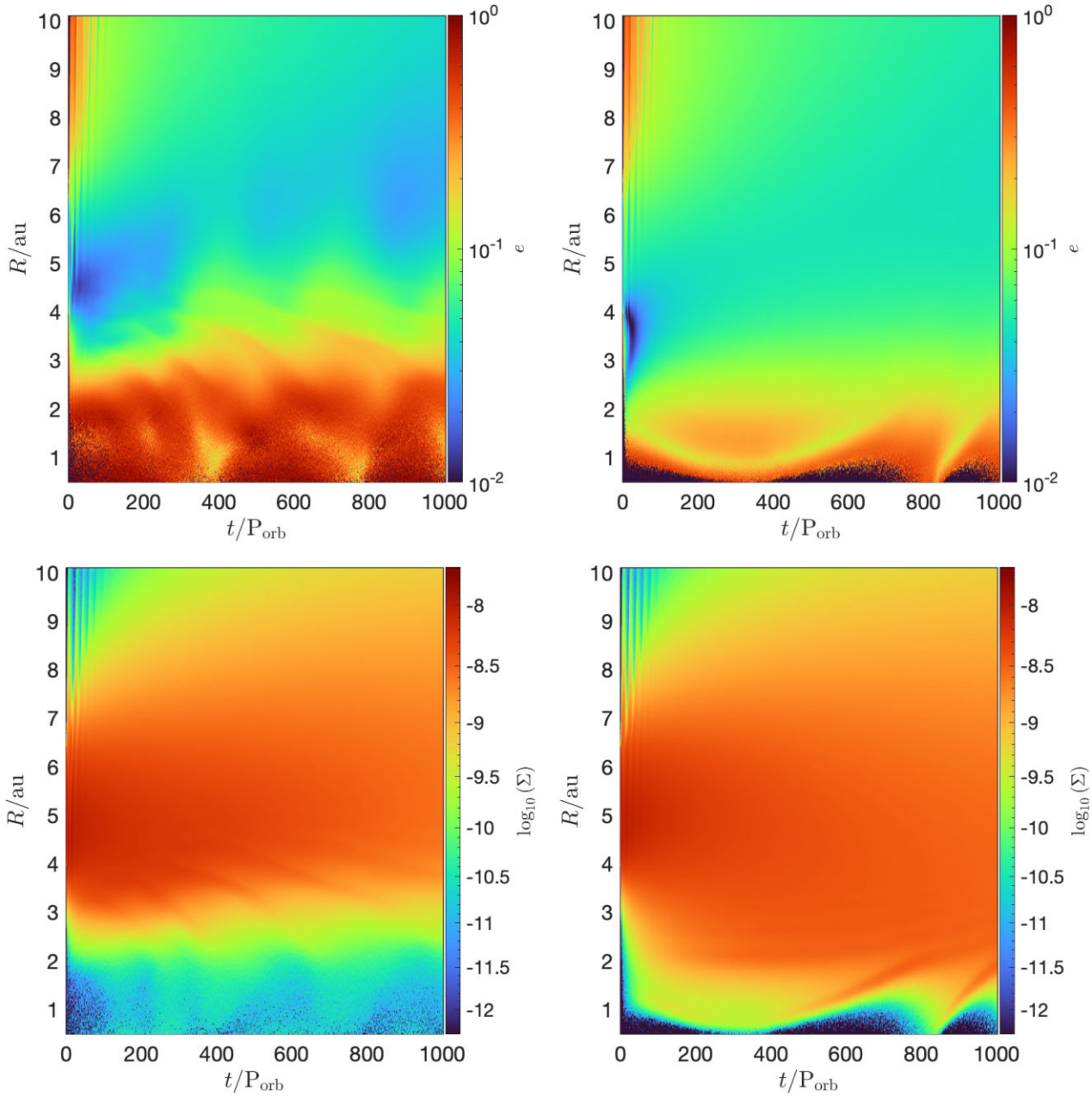
Figure 2. The disc eccentricity evolution for a coplanar disc (upper left panel, run1 from Table 1) and polar disc (upper right panel, run4). The *x* and *y* axes give the time in binary orbital periods, P_{orb}, and disc radius, *r*, respectively. The upper colour bars denote the disc eccentricity value, *e*. Eccentric material arises within the coplanar disc that is not present in the polar disc. The bottom left and right-hand panels show the disc surface density evolution for an initial disc tilt of coplanar and polar, respectively. The lower colour bars denote the disc surface density value, Σ. The disc that is initially polar is able to have stable material closer to the binary due to a weaker binary torque exerted on to the disc at a given radius.

polar disc than in the coplanar disc, as expected. Such eccentric disc behaviour around a binary at a similar binary eccentricity has been found previously, as discussed in Section 1. The cause of the disc eccentricity is not known. It could be due to tidal resonances with the binary (Lubow 1991).

Fig. 3 shows the global disc structure for both coplanar (left column) and polar (right colmun) orientations at $t = 300\,P_{orb}$ and $400\,P_{orb}$, respectively. For the coplanar model, there are prominent spiral streams transporting material from the circumbinary disc through the binary cavity and eventually accreting on to the binary. At $t = 300\,P_{orb}$ the strong stream is flowing dominantly on to the secondary companion, while at $t = 400\,P_{orb}$ the stream is being

dominantly accreted by the primary. For the polar model, no prominent streams are observed. Again, as expected, the cavity is larger in the coplanar case.

Another difference between the two disc structures is a prominent asymmetric density enhancement that arises within the coplanar disc but not the polar disc. This density feature is associated with the circumbinary disc becoming eccentric. The eccentricity is the largest at the disc's inner edge and then decreases in the outward radial direction (Fig. 2). This structure is a consequence of the trapped eccentric mode structure within a circumbinary disc (Shi et al. 2012; Muñoz & Lithwick 2020). We do not find the more detailed figure-eight like structures reported in 2D simulations by Mösta et al.
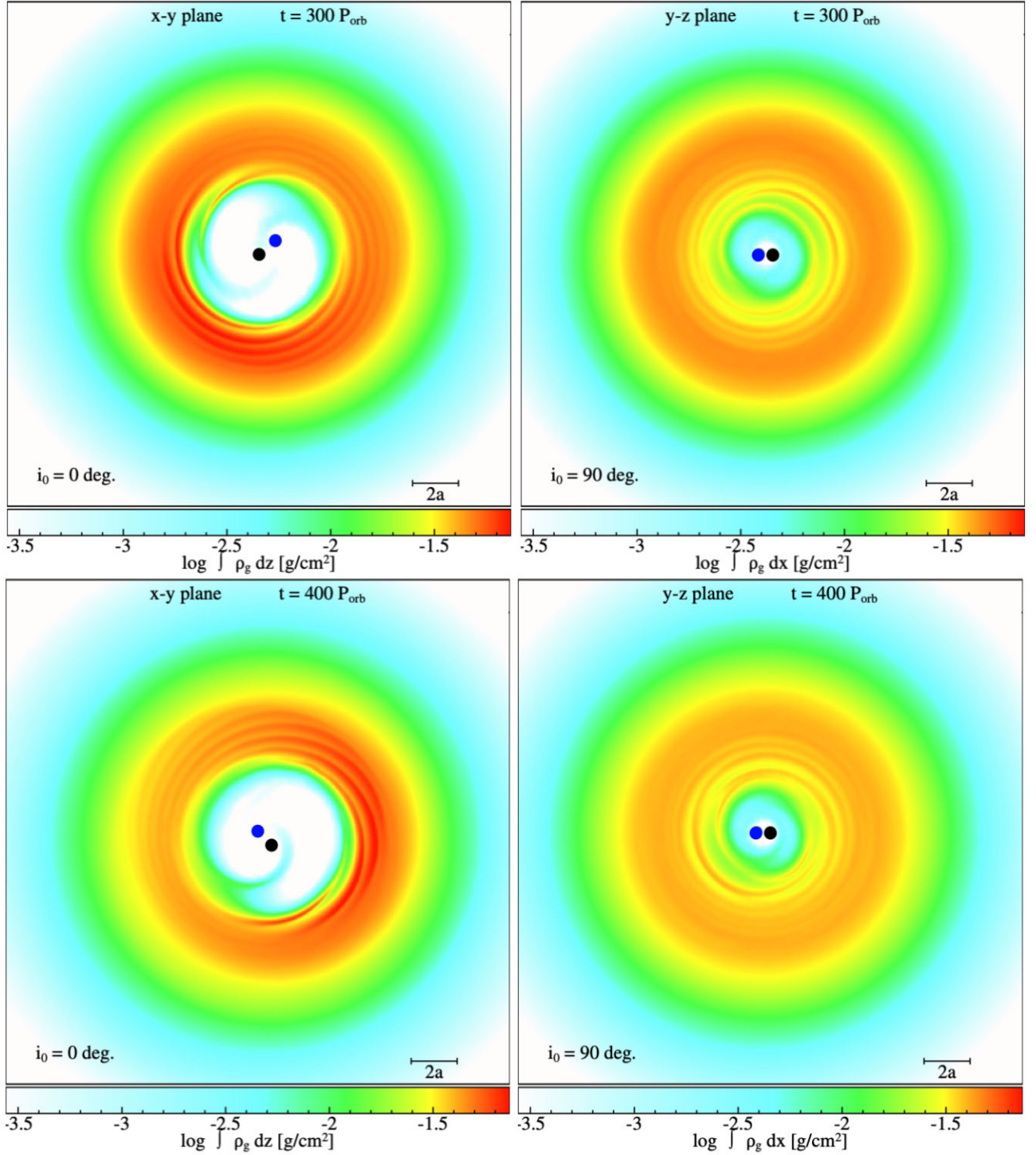
Figure 3. The disc evolution for a hydrodynamical circumbinary disc at times $t = 300\,P_{orb}$ (top row) and $400\,P_{orb}$ (bottom row). The left-hand panels show a disc that is coplanar ($i_0 = 0°$, run1 from Table 1) and the right-hand panels show a disc that is polar ($i_0 = 90°$, run4) to the binary orbital plane. The binary components are denoted by the circles with binary semimajor axis $a = 1$ au. The black circle represents the primary star and the blue denotes the secondary star. The colour bar denotes the gas surface density. The coplanar disc is viewed looking down on the binary orbital plane, the x–y plane. The polar disc is viewed in the y–z plane. In both cases, the binary eccentricity vector is along the x-axis. At a time of $t = 300\,P_{orb}$, a strong accretion stream can be seen flowing on to the secondary companion, while at $t = 400\,P_{orb}$, the stream is flowing on to the primary.

(2019). This may be because our simulations do not run as long and have lower spatial resolution in the gap region. On the other hand, these features may be less prominent in 3D that our simulations use.

3.2 Accretion rates

Next, we examine the accretion rates on to the primary and secondary stars for the coplanar and polar disc models. The upper panel of
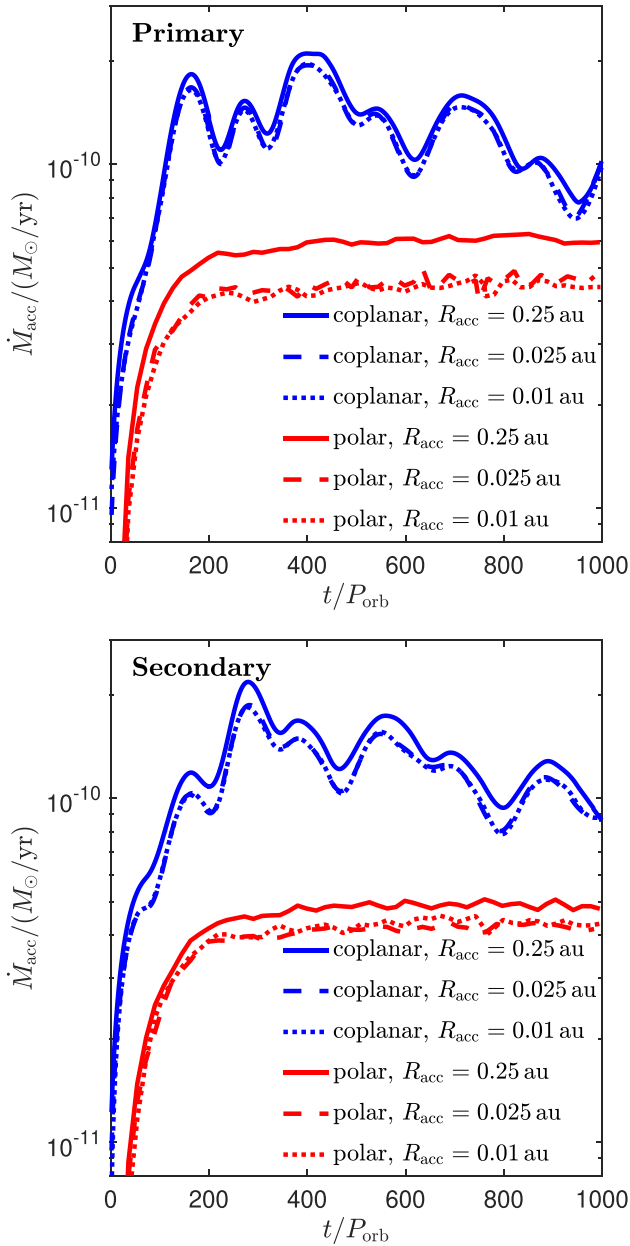
Figure 4. The accretion rate, $\dot{M}_{\rm acc}$, on to the primary star (top panel) and secondary star (bottom panel) as a function of time in units of the binary orbital period for a our coplanar and a polar disc models. The accretion rate is measured in solar mass per year, $M_\odot\,{\rm yr}^{-1}$. The disc orientation and accretion radius of each binary component is given by the legend.

Fig. 4 shows the accretion rate, $\dot{M}_{\rm acc}$, on to the primary star as a function of time. For the both disc models, we test three different accretion radii $R_{\rm acc} = 0.25$, 0.025, 0.01 au. In these simulations, the accretion rate initially increases over time due to the disc's inner parts viscously spreading inwards. The simulations with different accretion radii show similar rates, and so the accretion rate is approximately independent of the accretion radius. The accretion rate reaches a quasi-steady state in a time of about $150\text{–}200\,P_{\rm orb}$. No true steady state is possible because each disc loses mass over time. At a time of $1000\,P_{\rm orb}$ the coplanar disc has lost about 20 per cent of its initial mass, while the polar disc has lost about 15 per cent.

The last column in Table 1 shows the time-averaged accretion rates on to the primary and secondary binary components. For the coplanar models, the time-averaged accretion rate on to the primary is similar to the rate on to the secondary when averaged over the oscillations. For the polar models, the accretion rates on to the binary with the largest accretion radius are less than a factor of 1.4 greater than the smallest accretion radius. Again showing that the accretion rate does not depend strongly on the accretion radii of the stars.

In the coplanar case, the accretion rates on to the primary and secondary oscillate after a time of about $150\,P_{\rm orb}$, while the global accretion rate decreases over time. The oscillations in accretion rate are due to the apsidal precession of the circumbinary disc after it becomes eccentric (see Fig. 2) and occurs on a time-scale of $\sim 150\,P_{\rm orb}$. The accretion rates on to the primary and secondary are antiphased. That is, the accretion rate on to the primary is at a maximum when the accretion rate on to the secondary is at a minimum. Such oscillations, with a similar oscillation time-scale, were found in previous work (e.g. Dunhill et al. 2015; Muñoz & Lai 2016; Muñoz et al. 2019).

In the polar case, no significant accretion oscillations occur and the disc retains its nearly circular form. The accretion rate in the polar case does not decrease in time over the simulated time range, but must eventually decrease in time as the circumbinary disc mass becomes depleted. The accretion rates on to the primary and secondary are nearly equal. At a time of $1000\,P_{\rm orb}$, the binary accretion rate in the coplanar case is about a factor of two larger than in the polar case.

The gap sizes in the coplanar and polar cases are quite different (see Fig. 3), although the accretion rates are somewhat similar and appear to be approaching each other. This result may suggest that these cases are evolving towards steady state accretion through the circumbinary disc and into the gap (averaged over short time-scale accretion modulations), as has been suggested in recent studies (e.g. Muñoz et al. 2019; Dittmann & Ryan 2022). In such cases, the accretion rate on to the binary would then be independent of the binary properties and resulting gap size.

4 EFFECT OF THE OUTER COMPANION HD 98800 A

HD 98800 B is part of a quadruple system (as described in Section 1). We run an additional simulation including the HD 98800 A outer companion in order to examine the effect that it has on the accretion rate on to the B binary. We simulate a polar circumbinary disc around the HD 98800 B binary using the same disc and binary parameters as in Section 2. We model the HD 98800 A binary as a single star by combining the masses of the individual Aa and Ab stars. We set the semimajor axis and eccentricity to $a_{\rm A} = 54$ au and $e_{\rm A} = 0.52$, respectively (Kennedy et al. 2019). We calculate the tilt $i_{\rm A}$, argument of the pericentre $\omega_{\rm A}$, and longitude of the ascending node $\Omega_{\rm A}$ of HD 98800 A in the AB frame based on the binary properties in the sky plane from Kennedy et al. (2019). We find that $i_{\rm A} = 34°$, $\omega_{\rm A} = 137°$, and $\Omega_{\rm A} = 125°$. We use an accretion radius of 0.25 au for the B binary components, and use 1.85 au for the A companion. The outer companion does not significantly affect the disc dynamics for this system because the inner binary torque on the disc dominates the outer companion torque (Verrier & Evans 2009; Martin et al. 2022).

Fig. 5 shows the disc tilt and eccentricity, as well as the accretion rate to the B binary components, as a function of time in units of the B binary orbital period. We show the times of the periastron passage of HD 98800A by the vertical dotted lines. During each periastron passage, the disc tilt decreases by a few degrees and then increases soon after the periastron of the A companion. This may be why we observe the disc tilt to be $\sim 87°$ rather than exactly polar. Shortly after
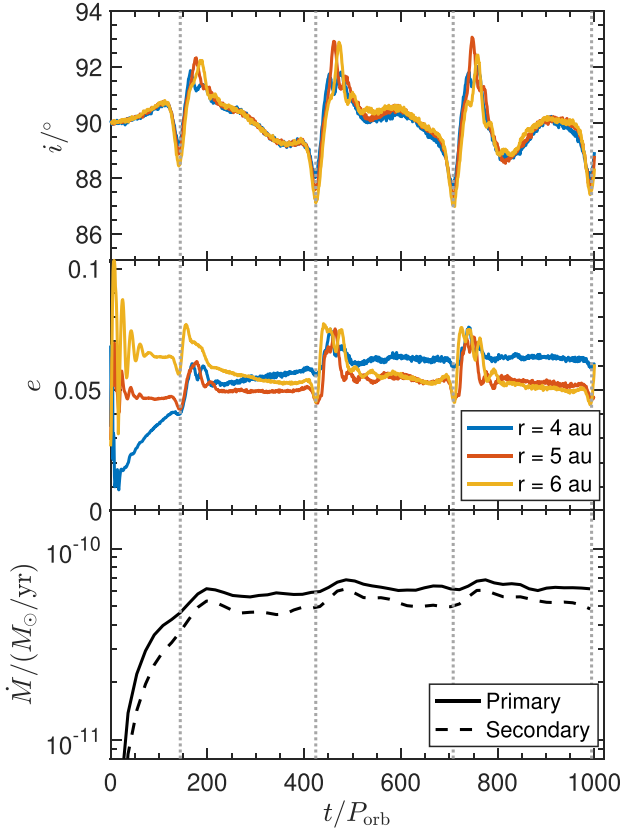
Figure 5. The evolution of the disc tilt, i, eccentricity, e, and accretion rate, $\dot{M}_{\rm acc}$, as a function of time in units of the binary orbital period in the presence of the HD 98800 A companion. For the disc tilt and eccentricity, we measure three different radii within the disc, $r = 4, 5, 6$ au. The accretion rate on to the primary is shown by the solid line, while the secondary is shown by the dashed line. The vertical grey dotted lines represent the time of periastron passages for HD 98000 A.

the periastron passage, the companion excites eccentricity growth in the polar circumbinary disc, temporarily enhancing the accretion rate. The accretion rate is of the order of $10^{-11} {\rm M}_\odot \, {\rm yr}^{-1}$, which is comparable to the simulation without the outer companion. However, the accretion rate modulates in time, increasing by $\sim$20 per cent after each periastron encounter of the companion. The primary accretion is higher than the secondary accretion, which is consistent with our previous simulations.

We analyse the global disc structure during the time of the closest approach of the A companion. Fig. 6 shows the disc structure at $424\,P_{\rm orb}$ (periastron, left-hand panel) and $462\,P_{\rm orb}$ (shortly after periastron passage, right-hand panel). There are no observed changes in the overall disc structure when the companion is at periastron. However, shortly after periastron, the companion excites prominent spiral arms in the disc, which temporarily enhances the accretion rate (see Fig. 5).

5 ACCRETION ON TO HD 98800 BABB

Observationally, $\dot{M}_{\rm acc}$ can be estimated by measuring the flux of continuum and line emission that is due to the shock of infalling gas from a disc on to the central star along the stellar magnetic field lines (e.g. Calvet & Gullbring 1998). The release of the accretion energy from the shock in the form of line emission is also known

as the accretion luminosity $L_{\rm acc}$ (Gullbring et al. 1998; Hartmann et al. 1998). The accretion luminosity $L_{\rm acc}$ is often computed from empirical relations between line luminosity, $L_{\rm line}$, and $L_{\rm acc}$ (e.g. Natta, Testi & Randich 2006; Biazzo et al. 2012; Fang et al. 2013; Antoniucci et al. 2014; Manara et al. 2015).

From observations, the emission line fluxes $F_{\rm line}$ can be calculated from the calibrated spectrum. From this, the line luminosities are given by

$$L_{\rm line} = 4\pi D^2 F_{\rm line} \qquad (2)$$

(Rigliaco et al. 2012), where D is the distance to the source. The accretion luminosities can be determined by using the measured line fluxes according to empirical relations between the observed line luminosities and the accretion luminosity or mass accretion rates (Gullbring et al. 1998; Natta et al. 2004; Mohanty, Jayawardhana & Basri 2005; Herczeg & Hillenbrand 2008; Fang et al. 2009). The empirical relationships were calibrated on small samples of well-observed T Tauri stars and brown dwarfs (Gullbring et al. 1998; Muzerolle et al. 2003; Calvet et al. 2004). The distance to HD 98800 BaBb is $D = 47\,{\rm pc}$ (van Leeuwen 2007). The brightest component has a H α flux of $6.5 \times 10^{-16}\,{\rm L}_\odot$ (Zurlo et al. 2020). Given this flux value, the line luminosity is $L_{\rm line} = 4.6 \times 10^{-8}\,{\rm L}_\odot$ (Zurlo et al. 2020).

The empirical relationship for $L_{\rm acc}$ based on $L_{\rm line}$ is given by

$$\log(L_{\rm acc}/{\rm L}_\odot) = b + a \times \log(L_{\rm line}/{\rm L}_\odot) \qquad (3)$$

(Rigliaco et al. 2012), where a and b are the line luminosity versus accretion luminosity relationships for selected accretion indicators (e.g. Fang et al. 2009). The accretion indicator that we are interested in is the H α line. Given that $a = 1.49$ and $b = 2.99$ for the H α line and $L_{\rm line} = 4.6 \times 10^{-8}\,{\rm L}_\odot$, the accretion luminosity for the brightest component in HD 98800 BaBb is $L_{\rm acc} = 1.14 \times 10^{-8}\,{\rm L}_\odot$. This value agrees with the findings of the accretion luminosity from Zurlo et al. (2020). Once $L_{\rm acc}$ is estimated, it can be converted into a mass accretion rate, $\dot{M}_{\rm acc}$, given by

$$\dot{M}_{\rm acc} = \left(1 - \frac{R_*}{R_{\rm in}}\right)^{-1} \frac{L_{\rm acc} R_*}{G M_*} \qquad (4)$$

(Rigliaco et al. 2012), where G is the universal gravitational constant, $R_\star$ is the radius of the star, and $R_{\rm in}$ is the inner truncation radius for the disc. The binary components will accrete material from a circumstellar discs that is continuously fed by a circumbinary disc. The factor $\left(1 - \frac{R_*}{R_{\rm in}}\right)^{-1} \sim 1.25$ is estimated using $R_{\rm in} \sim 5\,R_*$, which assumes that the accretion gas falls on to the star from the truncation radius of the circumstellar disc (e.g. Gullbring et al. 1998). Using $L_{\rm acc} = 1.14 \times 10^{-8}\,{\rm L}_\odot$, $R = 1.09\,{\rm R}_\odot$, and $M_* = 0.699\,{\rm M}_\odot$ (Boden et al. 2005), we estimate the mass accretion to be $6.8 \times 10^{-16}\,{\rm M}_\odot \, {\rm yr}^{-1}$.

For comparison, the accretion rates for single T Tauri stars are typically in the range of $\sim 10^{-10} - 10^{-7}\,{\rm M}_\odot \, {\rm yr}^{-1}$ (Valenti, Basri & Johns 1993; Gullbring et al. 1998; Calvet et al. 2004; Ingleby et al. 2013). Observations reveal accretion rates on to binary star systems are comparable to that of accretion rates on to single T Tauri stars (White & Ghez 2001). Binary components and single stars of similar mass have similar mass accretion rates. However, it has been shown that more massive stars generally have larger accretion rates than less massive stars (White & Ghez 2001). In HD 98800 BaBb, only the primary star (the slightly more massive binary component) has detectable H α flux.

The mass accretion rate on to the primary from the simulation of a polar disc with the HD 98800 A companion (run7) is $\sim 6 \times 10^{-11} {\rm M}_\odot \, {\rm yr}^{-1}$. Given that $\dot{M} \propto \alpha (H/R)^2$, a reduction in α and H/R is needed to obtain the observed accretion rate of
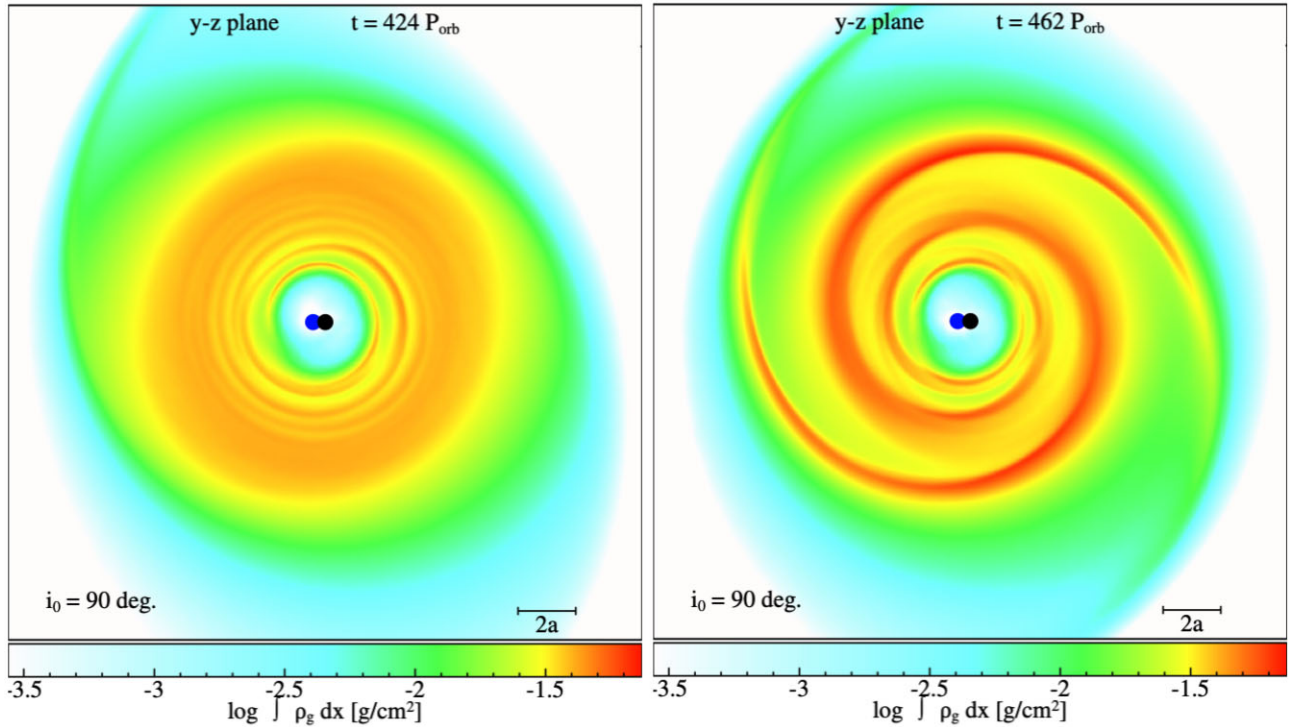
Figure 6. The disc evolution for a polar circumbinary disc around HD 98800 BaBb perturbed by HD 98800 A (run7) at times $t = 424\,P_{\rm orb}$ (periastron passage of HD 98800 A, left-hand panel) and $462\,P_{\rm orb}$ (time shortly after periastron, right-hand panel). The black circle represents the primary star and the blue denotes the secondary star. The colour bar denotes the gas surface density. The circumbinary disc is viewed in the y–z plane, with the binary eccentricity vector is along the x-axis. At a time of $t = 462\,P_{\rm orb}$, prominent spiral arms are formed by HD 98800 A.

$\sim 7 \times 10^{-16}\,{\rm M_\odot\,yr^{-1}}$ for the HD 98800 BaBb polar circumbinary disc. Therefore, we require $\alpha < 10^{-5}$ and $H/R < 0.05$. Such low values would be inconsistent with the tilt evolution time-scale to a polar state. Linear models in Lubow & Martin (2018) suggest a tilt evolution time-scale of $\tau \sim 5 \times 10^4 (H/R)^2/\alpha$ yr that could exceed the age of the system that is estimated as $\sim 10^7$ yr (Kennedy & Kenyon 2009; Ronco et al. 2021) (non-linear effects could reduce this time-scale). Our models also predict that the accretion rate on to the secondary is about the same as the accretion rate on to the primary. Therefore it is unclear why emission from only the primary is detected.

6 CONCLUSIONS

We have simulated the accretion of coplanar and polar circumbinary gas on to a highly eccentric binary with a mass ratio close to unity. For the same disc properties, except inclination, both the coplanar disc and polar disc accrete on to the primary and secondary stars at similar rates when averaged over many binary orbital periods. The polar disc has significantly different properties from the coplanar disc (e.g., Poblete, Cuello & Cuadra 2019). Unlike the coplanar disc, the eccentricity of the polar disc does not grow. For a coplanar disc, the accretion rates on to the binary components undergo oscillations so that the dominant accretion alternates between the components as a consequence of the precession of the eccentric disc, as was previously found (Dunhill et al. 2015; Muñoz & Lai 2016; Muñoz et al. 2019). However, for a polar disc, no such oscillations are found as a consequence of its persistent nearly circular form.

We applied our findings to the eccentric binary system, HD 98800 BaBb, which contains a polar circumbinary gas disc. We

include the outer companion HD 98800 A to determine its effects on the accretion rate on to the B binary during the periastron passage of the A companion. We found that the eccentric orbit of HD 98800 A increases the accretion rate on to HD 98800 B by ~ 20 per cent after each periastron passage. Using the observations from Zurlo et al. (2020), we estimated the primary mass accretion rate to be $\dot{M}_{\rm acc} = 6.8 \times 10^{-16}\,{\rm M_\odot\,yr^{-1}}$. This accretion rate is about 6 orders of magnitude lower than observations of accretion rates in T Tauri stars. Our hydrodynamical simulations are unable to explain such a low accretion rate unless the α parameter is very small, $\alpha < 10^{-5}$. Furthermore, we predict similar accretion rates on to both binary components, while observational signatures of accretion were found for only the primary. Further observational checks on the accretion rate would help to clarify these differences.

DATA AVAILABILITY

The data supporting the plots within this article are available on reasonable request to the corresponding author. A public version

of the PHANTOM and SPLASH codes are available at https://github.com/danieljprice/phantom and http://users.monash.edu.au/~dprice/splash/download.html, respectively.

REFERENCES

Aly H., Lodato G., 2020, MNRAS, 492, 3306
Aly H., Dehnen W., Nixon C., King A., 2015, MNRAS, 449, 65
Andrews S. M., Czekala I., Wilner D. J., Espaillat C., Dullemond C. P., Hughes A. M., 2010, ApJ, 710, 462
Antoniucci S., García López R., Nisini B., Caratti o Garatti A., Giannini T., Lorenzetti D., 2014, A&A, 572, A62
Artymowicz P., Lubow S. H., 1994, ApJ, 421, 651
Artymowicz P., Lubow S. H., 1996, ApJ, 467, L77
Beuzit J. L. et al., 2019, A&A, 631, A155
Bi J. et al., 2020, ApJ, 895, L18
Biazzo K., Alcalá J. M., Covino E., Frasca A., Getman F., Spezzi L., 2012, A&A, 547, A104
Boden A. F. et al., 2005, ApJ, 635, 442
Brinch C., Jørgensen J. K., Hogerheijde M. R., Nelson R. P., Gressel O., 2016, ApJ, 830, L16
Calvet N., Gullbring E., 1998, ApJ, 509, 802
Calvet N., Muzerolle J., Briceño C., Hernández J., Hartmann L., Saucedo J. L., Gordon K. D., 2004, AJ, 128, 1294
Chiang E. I., Murray-Clay R. A., 2004, ApJ, 607, 913
Czekala I., Chiang E., Andrews S. M., Jensen E. L. N., Torres G., Wilner D. J., Stassun K. G., Macintosh B., 2019, ApJ, 883, 22
D'Orazio D. J., Haiman Z., MacFadyen A., 2013, MNRAS, 436, 2997
Dittmann A. J., Ryan G., 2022, MNRAS, 513, 6158
Doğan S., Nixon C., King A., Price D. J., 2015, MNRAS, 449, 1251
Dunhill A. C., Cuadra J., Dougados C., 2015, MNRAS, 448, 3545
Duquennoy A., Mayor M., 1991, A&A, 248, 485
Facchini S., Lodato G., Price D. J., 2013, MNRAS, 433, 2142
Facchini S., Juhász A., Lodato G., 2018, MNRAS, 473, 4459
Fang M., van Boekel R., Wang W., Carmona A., Sicilia-Aguilar A., Henning T., 2009, A&A, 504, 461
Fang M., Kim J. S., van Boekel R., Sicilia-Aguilar A., Henning T., Flaherty K., 2013, ApJS, 207, 5
Farris B. D., Duffell P., MacFadyen A. I., Haiman Z., 2014, ApJ, 783, 134
Foucart F., Lai D., 2014, MNRAS, 445, 1731
Franchini A., Lubow S. H., Martin R. G., 2019, ApJ, 880, L18
Gullbring E., Hartmann L., Briceño C., Calvet N., 1998, ApJ, 492, 323
Günther R., Kley W., 2002, A&A, 387, 550
Hartmann L., Calvet N., Gullbring E., D'Alessio P., 1998, ApJ, 495, 385
Herczeg G. J., Hillenbrand L. A., 2008, ApJ, 681, 594
Ingleby L. et al., 2013, ApJ, 767, 112
Kennedy G. M., Kenyon S. J., 2009, ApJ, 695, 1210
Kennedy G. M. et al., 2012, MNRAS, 421, 2264
Kennedy G. M. et al., 2019, Nat. Astron., 3, 230
Kraus S. et al., 2020, Science, 369, 1233
Larwood J. D., Nelson R. P., Papaloizou J. C. B., Terquem C., 1996, MNRAS, 282, 597
Lodato G., Price D. J., 2010, MNRAS, 405, 1212
Lodato G., Pringle J. E., 2007, MNRAS, 381, 1287
Lubow S. H., 1991, ApJ, 381, 259
Lubow S. H., Artymowicz P., 2000, in Mannings V., Boss A. P., Russell S. S., eds, Protostars and Planets IV. Univ. Arizona Press, Tucson, AZ, p. 731
Lubow S. H., Martin R. G., 2018, MNRAS, 473, 3733
Lubow S. H., Ogilvie G. I., 2000, ApJ, 538, 326
Lubow S. H., Martin R. G., Nixon C., 2015, ApJ, 800, 96
Manara C. F., Testi L., Natta A., Alcalá J. M., 2015, A&A, 579, A66
Martin R. G., Lubow S. H., 2017, ApJ, 835, L28
Martin R. G., Lubow S. H., 2018, MNRAS, 479, 1297
Martin R. G., Lubow S. H., 2019, MNRAS, 490, 1332
Martin R. G., Lepp S., Lubow S. H., Kenworthy M. A., Kennedy G. M., Vallet D., 2022, ApJ, 927, L26
Miranda R., Lai D., 2015, MNRAS, 452, 2396
Miranda R., Muñoz D. J., Lai D., 2017, MNRAS, 466, 1170
Mohanty S., Jayawardhana R., Basri G., 2005, ApJ, 626, 498
Mösta P., Taam R. E., Duffell P. C., 2019, ApJ, 875, L21
Muñoz D. J., Lai D., 2016, ApJ, 827, 43
Muñoz D. J., Lithwick Y., 2020, ApJ, 905, 106
Muñoz D. J., Miranda R., Lai D., 2019, ApJ, 871, 84
Muzerolle J., Hillenbrand L., Calvet N., Briceño C., Hartmann L., 2003, ApJ, 592, 266
Natta A., Testi L., Muzerolle J., Randich S., Comerón F., Persi P., 2004, A&A, 424, 603
Natta A., Testi L., Randich S., 2006, A&A, 452, 245
Nixon C. J., 2012, MNRAS, 423, 2597
Nixon C. J., Cossins P. J., King A. R., Pringle J. E., 2011, MNRAS, 412, 1591
Nixon C., King A., Price D., 2013, MNRAS, 434, 1946
Papaloizou J. C. B., Lin D. N. C., 1995, ApJ, 438, 841
Papaloizou J. C. B., Pringle J. E., 1983, MNRAS, 202, 1181
Poblete P. P., Cuello N., Cuadra J., 2019, MNRAS, 489, 2204
Poon M., Zanazzi J. J., Zhu W., 2021, MNRAS, 503, 1599
Price D. J., 2007, PASA, 24, 159
Price D. J., Federrath C., 2010, MNRAS, 406, 1659
Price D. J. et al., 2018, PASA, 35, e031
Raghavan D. et al., 2010, ApJS, 190, 1
Rigliaco E., Natta A., Testi L., Randich S., Alcalà J. M., Covino E., Stelzer B., 2012, A&A, 548, A56
Ronco M. P., Guilera O. M., Cuadra J., Miller Bertolami M. M., Cuello N., Fontecilla C., Poblete P., Bayo A., 2021, ApJ, 916, 113
Schmid H. M. et al., 2018, A&A, 619, A9
Shakura N. I., Sunyaev R. A., 1973, A&A, 24, 337
Shi J.-M., Krolik J. H., Lubow S. H., Hawley J. F., 2012, ApJ, 749, 118
Smallwood J. L., Lubow S. H., Franchini A., Martin R. G., 2019, MNRAS, 486, 2919
Smallwood J. L., Franchini A., Chen C., Becerril E., Lubow S. H., Yang C.-C., Martin R. G., 2020, MNRAS, 494, 487
Smallwood J. L., Nealon R., Chen C., Martin R. G., Bi J., Dong R., Pinte C., 2021a, MNRAS, 508, 392
Smallwood J. L., Martin R. G., Lubow S. H., 2021b, ApJ, 907, L14
Tokovinin A., 2014a, AJ, 147, 86
Tokovinin A., 2014b, AJ, 147, 87
Valenti J. A., Basri G., Johns C. M., 1993, AJ, 106, 2024
van Leeuwen F., 2007, A&A, 474, 653
Verrier P. E., Evans N. W., 2009, MNRAS, 394, 1721
White R. J., Ghez A. M., 2001, ApJ, 556, 265
Zanazzi J. J., Lai D., 2018, MNRAS, 473, 603
Zúñiga-Fernández S. et al., 2021, A&A, 655, A15
Zurlo A. et al., 2020, A&A, 633, A119

This paper has been typeset from a TeX/LaTeX file prepared by the author.